REVISION 1

Structural investigation of (130) twins and rutile precipitates in chrysoberyl crystals from Rio das Pratinhas in Bahia (Brazil)

Sandra Drev,[1] Matej Komelj,[1] Matjaž Mazaj,[2] Nina Daneu[1] and Aleksander Rečnik[1]

[1] *Department for Nanostructured Materials, Jožef Stefan Institute, Jamova cesta 39, 1000 Ljubljana, Slovenia*
[2] *Laboratory for Inorganic Chemistry, National Institute of Chemistry, Hajdrihova 19, 1000 Ljubljana, Slovenia*

Abstract. We studied V-shaped twins of chrysoberyl ($BeAl_2O_4$) from Rio das Pratinhas pegmatites near Arataca in the Bahia state of Brazil. The local structure of the twin boundaries was determined using powder X-ray diffraction analysis (XRD), transmission electron microscopy (TEM) methods and density functional theory (DFT) calculations. To provide the most reliable model for DFT and HRTEM simulations the structure of chrysoberyl was first refined in the orthorhombic space group 62 (*Pmnb*) with unit cell parameters: a = 5.4825(1) Å, b = 9.4163(2) Å and c = 4.4308(1) Å, with 0.5 at% of Fe^{3+} present on the Al(2) sites, suggesting an average composition of $BeAl_{1.99}Fe_{0.01}O_4$. TEM study of V-shaped twins showed that the twin boundary lies in the (130) planes, and the angle measured between the crystal domains related by mirror twin operation is ~ 59.5°. Rigid structural model of (130) twin boundary in chrysoberyl was refined by DFT calculations, using a pseudo-potential method. The twin boundaries show local enrichment with Ti. Bulk chrysoberyl contains numerous nanosized TiO_2 precipitates with a distorted rutile structure, following the orientation relationship of $[001]_{Ch}\{120\}_{Ch}||[010]_R\{103\}_R$. The increase of Ti at the twin boundaries and the formation of rutile-type TiO_2 precipitates in bulk chrysoberyl suggest a transient Ti-exsolution that took place after the twin formation.

Keywords: chrysoberyl, alexandrite, Rietveld analysis, atomic structure, twinning, topotaxy

Introduction

Chrysoberyl ($BeAl_2O_4$) is a typical Be-mineral found in metamorphosed granite pegmatites (Franz and Morteani 1984). It occurs in association with quartz, beryl, alkali feldspars, muscovite, phenakite and other minerals depending on local geochemical and *p-T* conditions (Černý 2002). It commonly forms as a breakdown product of the primary pegmatitic beryl (Franz and Morteani 1984) at elevated temperatures (900°and 1200°C) and pressures (10 to 25 kbar) in the presence of water (Cemič *et al*. 1986). In pegmatites, it is generally found in the form of small euhedral grains or larger idiomorphic crystals embedded in quartz-muscovite matrix (Cornejo and Bartorelli 2010).

Beryllium aluminate, chrysoberyl ($BeAl_2O_4$), crystallizes in the olivine-type structure, a hexagonal close-packed (*hcp*) analogue of the cubic (*ccp)* spinel ($MgAl_2O_4$) structure (Farrell *et al*. 1963). It has a slightly distorted O-sublattice with Al^{3+} and Be^{2+} ions partially occupying octahedral (½) and tetrahedral (¼) interstices. In the literature, there are several structure reports for chrysoberyl, which do not differ as much in the lengths of cell parameters as they do in the axial setting of the orthorhombic unit cell leading to a variety of possible space subgroups. The chrysoberyl structure was first studied by Bragg and Brown (1926). In their analysis the chrysoberyl structure was correlated with the *hcp* wurtzite and corundum structures of primary oxides, BeO and α-Al_2O_3, and *ccp* structure of $MgAl_2O_4$ spinel. The authors used a crystallographic setting where the orthorhombic *c*-axis is set parallel with the striations on the main pinaciodal faces, whereas the *a*-axis is parallel to the pseudo-hexagonal axis of the crystal (Rose 1839). Based on this axial setting they determined a space group V_h^{16}, which in Hermann-Mauguin notation corresponds to *Pbnm* (62). Later, the structure was refined in *Pnma* (62) space group (Swanson *et al.* 1960; Farrell *et al.* 1963), which corresponds to another crystallographic setting used in the 19th century (*e.g.* Schrauf 1877). In this setting, the orthorhombic *c*-axis is parallel to the pseudo-hexagonal axis of the crystal. Further setting that can be found in the literature refers to the *Pmnb* (62) space group (Palache *et al.* 1944, Tabata *et al.* 1974). Depending on the axial setting, the V-shaped twins of chrysoberyl are referred to as (031), (310) and (130), respectively. In addition to the simple contact twins, cyclic sixlings produced by repeated twinning around the pseudo-hexagonal axis are quite common (*e.g.* Rose 1839; Schmetzer 2010). Chrysoberyl crystals often contain inclusions of different minerals. When oriented, these inclusions scatter light along the specific orientation within the hosting crystal, known as cat's-eye effect or chatoyancy. Mitchell and Marder (1982) demonstrated that in chrysoberyl this effect is caused by oriented precipitation of rutile. Exsolution of precipitates in more than one direction causes a multiple chatoyancy or asterism, where the rays of light are intersecting at characteristic angles when viewed along special orientations. A similar effect is achieved in flux growth by doping chrysoberyl with titanium and annealing in

oxygen atmosphere. According to Schmetzer (2010) this effect is most likely caused by the exsolution of rutile. Until the present these structural peculiarities have not yet been studied in detail.

The challenge of our investigation was to solve the structure of simple contact twins and the origin of asterism in chrysoberyl at the atomic scale. For this purpose we used quantitative methods of X-ray diffraction, energy-dispersive X-ray spectroscopy, electron microscopy and image simulations supported with density functional theory calculations. For our study we used the V-shaped twins of chrysoberyl from Rio das Pratinhas, municipality of Arataca in Bahia, Brazil (de Souza *et al.* 2003).

Experimental methods

Sample description

V-shaped contact twin of chrysoberyl from Rio das Pratinhas, shown in Figure 1a, was used in our investigation of the twin boundary structure. The crystals have pale olive-green color and show a 2-ray asterism under the incident light when viewed along the pseudo-hexagonal axis. The crystals are symmetrically developed and show no attachment point suggesting that they grew as floaters. The twin boundary splits the crystal into two mirror-symmetric halves, enclosing an angle of ~59.5°.

Powder X-ray diffraction analysis

The crystal structure of chrysoberyl was determined on finely ground sample at an ambient pressure and temperature using a high-resolution X-ray diffractometer (XRD; PANalytical X'Pert PRO, Almelo, The Netherlands) with $Cu_{K\alpha 1}$ radiation (λ = 1.5406 Å) and fully opened 100 channel X'Celerator detector under a continuous scanning mode in 2θ range from 15 to 90° and a recording time of 300 s per step of 0.016°. The crystal structure was refined by Rietveld analysis of experimental X-ray diffractograms using the TOPAS-Academic V4 software package (Coelho Software, Brisbane, Australia). The background profile and the geometry of experimental XRD pattern were fitted by the Le Baile method before including the structure parameters. The atomic positions determined by R.M. Hazen (Hazen 1987) at an ambient pressure were used as the starting structure for our refinement. Rietveld

analysis was performed in the following sequence: refinement of the unit cell parameters, temperature factors, atomic positions and partial replacement of Al-sites by Fe, according to the experimental EDS data. At the final stage, Rietveld refinement involved 54 independent parameters.

Transmission electron microscopy

The crystals have a high density of cracks, which made the TEM sample preparation rather challenging. For our investigations the sample was cut from the central part of the crystal into square blocks of 1.8 x 1.8 mm along the pseudo-hexagonal axis containing the twin boundary at the centre (*see* Figure 1b). The blocks were fitted into 3 mm ceramic alumina cylinders using epoxy glue to improve strength. The TEM specimen cut from the centre of the sample was ground to a thickness of 100 µm and dimpled down to 20 µm at the disc centre (Dimple grinder, Gatan Inc., Warrendale PA, USA). TEM specimen was finally ion-milled (PIPS, Precision Ion Polishing System, Gatan Inc.) using 4 kV Ar^+ ions at an incidence angle of 8° until perforation. To enhance electron conductivity the specimen was finally coated by a few-nm-thick layer of amorphous carbon. Detailed structural investigations of the samples were performed using a conventional 200-kV transmission electron microscope (JEM-2100, Jeol Ltd., Tokyo, Japan) equipped with LaB_6 electron source and ultra high-resolution objective pole-piece having a point-to-point resolution of 0.19 nm, sufficient for resolving the lattice images of chrysoberyl along the pseudo-hexagonal zone-axis. Chemical analysis was performed using Si(Li) energy-dispersive spectroscopy (EDS) detector. HRTEM images were recorded on CCD camera using DigitalMicrograph™ (Gatan Inc., Pleasanton CA, USA) as a user interface. The super-cell models were constructed using IDL™ (Research Systems Inc., Boulder CO, USA) and CrystalMaker™ (CrystalMaker Software Ltd., Oxfordshire, UK), and finally, the HRTEM image simulations were performed using the EMS software package (P.A. Stadelmann, EPFL Lausanne, Switzerland).

Density functional theory calculations

Super-cell resulting from HRTEM analysis of the twin boundary was used as a starting model for relaxation of the atomic positions. Ab-inito calculations of the interatomic forces and the total energies were performed within the framework of the density-functional theory (DFT) by applying the Quantum Espresso code (Giannozzi *et al.* 2009) using the generalized-gradient approximation (GGA; Perdew and Zunger 1981). The effect of core electrons was taken into account in terms of projector-augmented-wave (PAW) pseudo-potentials (Blöchl 1994). The plane-wave cut-off parameters were

set to 204 eV and 1642 eV, respectively, whereas due to the size of the system the Kohn-Sham equations were solved for the gamma point only. The criterion for self-consistency was the total-energy difference between the two subsequent calculations being less than 10^{-7} Ry. The standard Broyden-Fletcher-Goldfarb-Shanno algorithm was applied to optimize the atomic positions by reducing the magnitude of the forces. During the calculation the atomic positions were relaxed by means of minimizing the interatomic forces, whereas the lattice parameters were kept constant in order to avoid the volume effect on the energy. The relaxation was completed when the sum of absolute values of all interatomic forces was less than 0.03 % of its initial value for the non-relaxed structure.

Results and discussion

The main challenge of our work was to determine the structure of V-shaped twins and the nature of inclusions causing asterism in chrysoberyl. For this purpose we first refined the crystal structure of chrysoberyl, which served for determining other subordinated structural features. Crystal structure determination is followed by the analysis of the twin boundary structure at the atomic scale using electron microscopy methods supported by ab-initio calculations and refinement of atomic positions at the twin interface. Finally, the nature of inclusions and their orientation relationship with chrysoberyl was investigated.

Crystallographic setting and refinement of the chrysoberyl structure

When studying the structure of interfaces the crystal structure of the main phase must be properly determined. Because of the persisting inconsistencies in the literature and in mineralogical databases regarding the index of the twin plane in chrysoberyl it appears necessary that crystallographic orientation of the orthorhombic unit cell is fixed in a way that it is consistent with other structurally related minerals.

Chrysoberyl belongs to the spinelloid group of minerals (Davies and Akaogi 1983). All minerals of this group can be derived from the spinel archetype structure through periodic twinning, which produces a stacking disruption in the O-sublattice, generating different modulated structures. The stacking disruption in these compounds is accompanied by a local departure from crystal chemistry. This principle is best demonstrated between spinel ($MgAl_2O_4$) and chrysoberyl ($BeAl_2O_4$). In both com-

pounds the cations occupy ¼ of the available interstices, located at ~1/3 (tetrahedral Type-I), ~1/2 (octahedral) and ~2/3 (tetrahedral Type-II) distance between the close-packed planes in the oxygen sublattice; ½ of the octahedral sites are occupied by Al^{3+}, whereas ¼ of the tetrahedral sites are occupied by Mg^{2+} or Be^{2+}. The main difference between the two structures arises from the stacking of the O-sublattice. In spinel, the close-packed planes in the O-sublattice are stacked in a cubic *ccp* sequence (ABC) along ⟨111⟩ directions of the structure, while in chrysoberyl the oxygen close-packed planes are stacked in hexagonal *hcp* sequence (ABA) along the pseudo-hexagonal axis. The comparison becomes even more interesting when the spinel structure is twinned. This operation generates a local *hcp* stacking, similar to that observed in chrysoberyl, in an otherwise perfect *ccp* lattice. Further it has been shown that twinning in spinel is accompanied by replacement of Mg^{2+} with Be^{2+} on tetrahedral sites adjacent to *hcp* planes in the O-sublattice (Daneu *et al.* 2007a, Drev *et al.* 2013), demonstrating that twinning is in fact chemically induced (Takeuchi 1997), which further facilitates the structural relationship between spinel and chrysoberyl. As a result of such structural (*ccp* → *hcp*) and chemical (Mg^{2+} → Be^{2+}) modulation, a range of minerals belonging to polysomatic taaffeite series exists between the two end-compounds: $Be_2Mg_2Al_8O_{16}$ (Anderson *et al.* 1951), $BeMg_3Al_8O_{16}$ (Moor *et al.* 1981), $BeMg_2Al_6O_{12}$ (Schmetzer 1981), and $Be_{1.33}Mg_{2.67}Al_8O_{16}$ (Schmetzer 1983) with general formula of $Be_xMg_yAl_{2(x+y)}0_{4(x+y)}$. In all these compounds, the crystallographic *c*-axis is oriented normal to close-packed O-layers (interlayer distance ~2.3 Å), while its length depends on a repeat sequence of *ccp* and *hcp* sheets (Anderson *et al.* 1951). Following this analogy, chrysoberyl can be described as the end-member of this series with the highest possible density of tropochemical twins, having fully evolved *hcp* structure, where all Mg^{2+} ions are being replaced by Be^{2+} ions (*see* Figure 2). Transposed into taaffeite orientation, the *c*-axis of chrysoberyl becomes parallel with the pseudo-hexagonal axis of the structure that corresponds to [111] of spinel, while its *b*- and *a*-axis correspond to $[11\bar{2}]$ and $[1\bar{1}0]$ of spinel, respectively. In this way, the structure of chrysoberyl can be directly compared with the spinel and taaffeite members of the series, as illustrated in Figure 2.

Experimental X-ray powder diffraction pattern of our sample was best matched with the crystal structure of chrysoberyl at the atmospheric pressure (Hazen 1987; JCPDS 01-078-0956), with minor reflections belonging to nanocrystalline rutile (Figure 3). The crystal structure of chrysoberyl from Pratinhas was refined in the orthorhombic *Pmnb* (62) space group, using starting structural model from Hazen (1987) with transposed crystallographic setting, according to the above consideration: *c* → *a* = 5.481 Å, *b* = 9.415 Å, *a* → *c* = 4.428 Å. Rietveld analysis of experimental XRD data included iterative refinement of unit-cell parameters, temperature factors and atom positions. Given that in addition to pressure (Hazen 1987) and temperature (Hazen and Finger 1987), the cell parameters of chrysoberyl vary also depending on the presence of impurities (Weber *et al.* 2007) the composition

of the sample was checked by EDS analysis, which showed a minor presence of Fe (*see* Section on electron microscopy). The inclusion of 0.01 at% Fe on Al(2)-sites notably improved the refinement, suggesting an average chemical composition of $BeAl_{1.99}Fe_{0.01}O_4$, whereas partial replacement of Al(1)-sites by Fe had no effect. In the final stage, nanocrystalline rutile was included as a minor secondary phase. The structure refinement of the rutile included in chrysoberyl was less reliable due to broad and weak reflections of rutile, which can be attributed to relatively low concentration of rutile in the bulk material, its small crystal size, and possibly large structural anisotropy. In the first step, Rietveld analysis involved the refinement of rutile's unit-cell parameters and crystal size. This was followed by taking into account preferential orientation of the rutile precipitates within the chrysoberyl crystals (indicated by HRTEM analysis) using spherical harmonics series. Because the exact atomic positions within the rutile precipitates, strained by the hosting chrysoberyl structure, are in fact unknown, only the temperature factors were relaxed for fixed atomic positions. Quantitative analysis including refined chrysoberyl and rutile structures resulted in 98.0(9) mol% of chrysoberyl and 2.0(9) mol% of nanocrystalline rutile with an average particle size of ~ 50 nm. Refined unit-cell parameters of the chrysoberyl crystals from Pratinhas are: a = 5.4825(1) Å, b = 9.4163(2) Å, c = 4.4308(1) Å (*s.g. Pmnb*, No.62), whereas those of rutile converged to a = 4.7331(4) Å, c = 2.880(2) Å (*s.g. $P4_2/mnm$*, No.136). The Rietveld refinement was stopped with R_{wp}, R_p, R_{Bragg} factors of 0.078, 0.058 and 0.025, respectively. Further details on crystal data, fractional coordinates, site occupancy, isotropic displacement parameters, interatomic distances and principal angles are given in Supplementary information. Comparison between experimental XRD pattern and calculated patterns for chrysoberyl and rutile are shown in Figure 3. Refined structure of chrysoberyl was used in the subsequent TEM analysis.

Atomic structure of (130) chrysoberyl twins

Crystallography and atomic structure of V-shaped twins in chrysoberyl were studied in detail by methods of transmission electron microscopy. According to determined crystallographic setting the specimens were investigated in [001]-projection, where the twin boundaries are viewed edge-on. Figure 4 shows a twin boundary with numerous precipitates found in two special orientations with respect to the crystal lattice of chrysoberyl. Slight deviations from their orientation are due to bending of the thin crystal foil in the low-magnification TEM image. When crossing the interface, the general orientation of precipitates is reflected, owing to special crystallographic relation between the two crystal domains in twin orientation. The twin boundary runs straight over large sections of the TEM sample, making occasional steps where it glides away to nearby parallel planes (Fig. 4b). Electron diffraction patterns (EDPs) recorded from adjacent crystal domains show common {260} reflec-

tions, indicating that the twin boundary lies parallel to the {130} planes of the chrysoberyl structure (*see* simulated EDP pattern of the twin in Fig. 4c). The angle measured between the a-axes corresponds to the calculated angle of 59.44° for (130) twin in our crystallographic setting (*Pmnb*). In different setting, the indexing of the twin plane would of course be different (*e.g.* Farrell *et al.* 1963; Schmetzer 2010). Faint intensities that can be seen in the experimental EDPs at the positions of forbidden reflections result from dynamic scattering and subsequent recombination of intensities in thicker crystal parts, whereas the net contribution to diffraction intensity from precipitates appears just too low to be seen in EDPs, even when recorded with the smallest selected area apertures.

Let us now focus on the atomic structure of (130) twin boundary. HRTEM images recorded in (001) zone axis around defocus value of -60 nm show an undulating bright chain-like pattern following O atomic columns, that remains stable over a wide thickness range of 10-25 nm. This condition is very sensitive to the positions of Be-atoms, which alternate from one to another side of the chain (*see* Figure 5). Following the interface, we observe that the periodicity is roughly attained after every ~1.9 nm, corresponding to $4 \cdot d_{110}$ interplanar distances. In such periodic features, the chains meet symmetrically at the interface where the twin plane acts as a mirror plane for the two crystal domains. In some sections of the interface, where the twin boundary glides to parallel (260) planes, the symmetry of this feature is broken. In such regions chain from one domain overshoots the other, depending in which direction the twin boundary is deflected. Many such situations can be seen when glancing along the slightly climbing twin interface in Figure 5a. In this study we focused on the symmetric (130) twin interface. For quantitative HRTEM analysis larger area of the interface was searched and periodic sections were averaged to enhance the fine contrast features of the experimental image. A close-up of averaged periodic parts of experimental image is shown in Figure 5b.

Serpentine-like chains (marked by undulating black lines in Fig. 5b) from the two domains that meet symmetrically at the interface produce two distinct features, designated as Cluster-I and Cluster-II. Cluster-I comprises one vertical bright lozenge followed by two parallel bright dots and the contrast of Cluster-II appears as its reverse (marked by short black lines in Fig. 5b). These two atomic clusters will be studied in detail as they carry important information on the local structure of the twin boundary. Based on image simulations of bulk chrysoberyl crystal gives us some idea about possible atomic arrangements at the interface. Be-atoms can be easily assigned for Cluster-I, whereas this is not so straightforward for Cluster-II. In order to better understand the local arrangement of atoms we designed atomic models of (130) twin boundary based on the observed contrast features. The models were constructed in form of orthorhombic super-cells with dimensions: $A = 16 \cdot d_{130} = 4.35824$ nm, $B = 4 \cdot d_{110} = 1.89516$ nm, $C = d_{001} = 0.44308$ nm, containing 451 atoms. There are two possible

operations that produce a symmetric twin boundary in (130) plane: (*i*) reflection, or (*ii*) 180° rotation around the interface normal pointing from any octahedral interstice of the O-sublattice. Any of these two operations produces the same result. Image simulations quite faithfully reproduce the features of bulk crystal domains, however the interface structure appears to be incorrect (Figure 5c). Instead of the expected lozenge-dots features Cluster-I appears as a circle and Cluster-II as an intense bright dot. The striking difference in these contrast features results from possibly different occupation of coordination polyhedra at the twin interface accompanied by some relaxation.

Image simulations, based on a simple mirror-twin model, match the contrast of bulk crystal parts, whereas the interface is not well reproduced and needs some reconstruction. To refine the atomic positions we employed calculations within the framework of the density functional theory (DFT), using pseudo-potential method. Although the use of these methods requires a full 3D periodicity of the investigated structures, it is possible with suitable handling of the boundary conditions to optimize also the non-periodic features such as twin boundaries and other interfaces. Theoretical calculations thus make possible to optimize the interface structures by relaxation of individual atomic positions. In the first step, a rigid atomic model, produced by simple mirror operation, was relaxed by minimizing the total interatomic forces. At this stage, the coordination of atoms was fixed in order to maintain the local charge balance and observe any large discrepancies from their central positions, which would indicate that they need to be displaced to an alternative site. Because of the break-down of the super-cell periodicity along its *A*-axis, this dimension was selected large enough to avoid the cell-edge interference with the (130) twin boundary structure. The large number of atoms significantly increased the computation time, while as a result atomic positions at the twin boundary were more reliably determined. Searching for the most favorable energy for each atom in its coordination resulted in significant displacements of Be^{2+} and O^{2-} atoms located at the twin boundary (*see* Figure 6). In Cluster-I, the upper pair of Be^{2+} atoms (Layer 2) shifted in [110]-direction towards the interface, whereas in Cluster-II, the central pair of Be^{2+} atoms (Layer 1) moved in $[0\bar{1}0]$-direction further away from the interface to the corners of tetrahedral (Type-I) interstices. Relaxed model is also showing a slight relaxation of other atom positions along the interface inside their coordination polyhedrons. While HRTEM simulations based on the intermediate model showed a good match for Cluster-I, the contrast of Cluster-II was still not reproduced, indicating that the two Be^{2+} atoms shall not be located in the existing interstices. A new DFT run with Be^{2+} atoms translated to the neighboring tetrahedral sites (Type-II) converged rapidly reducing the total free energy from the initial model by three orders of magnitude. The local charge balance involved with this operation remained unchanged. The resulting DFT refined super-cell model was used for HRTEM image simulations, which showed an excellent match with the experimental HRTEM image (Figure 5d). Not only that all general features of the two

atomic clusters are well reproduced, but also the fine details, such as weak connections between the ripples in the upper part of Cluster-I, and interrupted chain in the lower part of Cluster-II are present in the simulated image. It is quite astonishing that DFT calculations provided a model, which could be confirmed by quantitative HRTEM analysis through proper selection of imaging conditions that were sensitive to the positions of Be^{2+} atoms. The final atomic model is illustrated in Figure 6.

Recent studies in different minerals indicated that the presence of specific elements at the twin boundaries play a decisive role during the twin formation (Šrot *et al.* 2003; Daneu *et al.* 2007b; Drev *et al.* 2013; Daneu *et al.* 2014). The detection of twin-triggering element often presents a challenging analytical task, owing to its low amounts and difficulties of locating the nucleation core of twinned crystal where it is actually present (Rečnik and Daneu 2012). If detected, it is quite easily differentiated from other impurity elements that might be present in the bulk crystal near the twin boundary, because of its abrupt and highly organized appearance in specific interstices (Daneu *et al.* 2007b). Natural chrysoberyl crystals are prone to incorporate different foreign elements (Fe^{3+}, Cr^{3+}, $Ti^{4+/3+}$, *etc.*), which are mainly responsible for the optical properties. The well known alexandrite effect is caused by the replacement of Al^{3+} by Cr^{3+} and Fe^{3+} ions in the chrysoberyl structure (Scalvi *et al.* 2003; Weber *et al*. 2007; Schmetzer 2010). To study the chemistry of our samples we performed EDS analyses in bulk chrysoberyl, at the twin boundary and across the precipitates (Figure 7). Bulk chrysoberyl in different parts of the TEM sample consistently showed small quantities of Fe, which is a common natural impurity element in chrysoberyl crystals. Relative to Al the concentration of Fe in chrysoberyl amounts to 0.56 ± 0.09 at%. This is comparable to the fraction of Fe that produced the best match for bulk chrysoberyl structure in Rietveld analysis (*see* Crystallography section) and reported data on Fe-rich chrysoberyl from other localities (Lottermoser *et al.* 2011). The amount of Fe increases when approaching the twin boundary where it is accompanied by an increase of Ti. The presence of Ti could either be an effect of segregation, or it could be the element that actually triggered the formation of the twin boundary. A relatively large variation in Ti concentration along the twin boundary under otherwise identical acquisition conditions (spot size, specimen thickness, count rate, *etc.*) suggests that Ti most likely segregated to the twin boundary from bulk chrysoberyl on cooling. It is noteworthy that the majority of studies on the chrysoberyl synthesis also report on the formation of twinned crystals under seemingly very dissimilar processing conditions (Farrell and Fang 1964; Tabata *et al.* 1974; Khranenko and Yurkin 2000). Tabata *et al.* (1974) suggested that boron triggers the twinning of chrysoberyl, however other synthesis routes that also produced twinned crystals did not involve the addition of B_2O_3. Common to all these approaches is that the syntheses entailed the use of the primary oxides, BeO and Al_2O_3. Based on the recent studies of bixbyite (Kleebe and

Lauterbach 2008) and rutile (Daneu *et al.* 2007b; Daneu *et al.* 2014), there exists a possibility that also so in chrysoberyl the (cyclic) twinning could be initiated by epitaxial growth on precursor oxides.

Structural analysis of rutile precipitates in chrysoberyl

Numerous Ti-rich precipitates populating the hosting structure (*see* Figs. 4a and 7) suggest that some exsolution process took place after the formation of chrysoberyl crystals. Precipitates occur in a highly anisotropic, slab-like morphology, are few nanometers thick, and up to 50 nm long on average. They are oriented in two specific orientations with respect to chrysoberyl lattice (Figures 8a-c), occasionally coinciding to form obtuse L-shaped or acute V-shaped clusters, enclosing the angles of 98.7° and 81.3°, respectively. These correspond to the angles intersected by {120} planes of chrysoberyl lattice, suggesting that the precipitates exsolved along these specific planes. Due to their low concentration and small size, EDPs recorded over chrysoberyl matrix with precipitates did not show any additional reflections even when choosing the smallest 0.1 µm selected area aperture available on this particular microscope. Fast Fourier transforms (FFTs) of HRTEM images from larger precipitates indeed show faint reflections that could be assigned to rutile (Figure 8e), but their quality was not sufficiently high to allow a more accurate crystallographic analysis. HRTEM images were used instead to determine crystallographic relationship between chrysoberyl and rutile. As indicated by the angle between the precipitates, interface planes in chrysoberyl indeed coincide with $\{120\}_{Ch}$ planes. Chrysoberyl lattice was then used as a reference to determine the unit-cell parameters of deformed rutile, as illustrated in Figure 8d. The lattice images of the precipitates suggest that, like chrysoberyl, also the rutile is oriented along its pseudo-hexagonal axis, *i.e.* $[010]_R$ or $[100]_R$. To determine the orientation of *a* and *c*-axes, distances along the three pseudo-hexagonal directions of the rutile lattice were measured over several tens of lattice planes to ensure higher accuracy. The resulting interplanar distances were d_{101} = 0.2456 nm and d_{001} = 0.2875 nm, and hence the lattice parameters of rutile were calculated: *a* = 4.725 Å and *c* = 2.875 Å. The result surprisingly well matches the lattice parameters determined by Rietveld refinement taking into account the relatively low amount of the rutile phase (*see* the Crystallography section). Unit-cell dimensions, showing such a large expansion of the rutile structure along the *a*-axis and contraction along the *c*-axis, are quite unusual (Henderson *et al*. 2009; *a* = 4.5922 Å and *c* = 2.9576 Å at RT) and are a consequence of chrysoberyl lattice contraction on cooling (Hazen and Finger 1987) after the formation of precipitates. Based on measured deformation of rutile and taking into account the thermal expansion data for chrysoberyl and rutile we can estimate the exsolution temperature where both structures are unrestrained ($\Delta V(T)_R = 0$). Assuming that on cooling the rutile expansion is controlled by local contraction of the chrysoberyl lattice this temperature is ~ 970°C, which roughly falls in the lower range of

352 temperatures reported for the formation of chrysoberyl by metamorphic decomposition of
353 pegmatitic beryl (Cemič *et al*. 1986).

354 During phase separation process the morphology of precipitates is dictated by the lowest energy
355 interfaces between the two structures, where the longest dimensions of precipitates commonly cor-
356 respond to the best matching directions that exist between the two phases. In our case, Ch|R_1 inter-
357 face is composed of $(120)_{Ch}$ terminating plane of the chrysoberyl lattice and $(103)_{R1}$ of the rutile-I. As
358 no physical lattice planes exist normal to the Ch|R_1 interface, the misfit between the precipitate and
359 the host is best calculated using a linear combination of basic lattice vectors corresponding to inter-
360 face planes in chrysoberyl and rutile. If the interface planes are decomposed into the fractions of lat-
361 tice vectors, *i.e.* $(120)_{Ch} \equiv (½,⅓,0)_{Ch}$ and $(103)_{R1} \equiv (⅓,0,⅓)_{R1}$, the distances between the coincident in-
362 terface points, d_{Ch} and d_R, are given by: $d_{Ch}^2 = (2\cdot a_{Ch})^2 + b_{Ch}^2$ and $d_R^2 = (3\cdot a_R)^2 + c_R^2$. Calculated for lat-
363 tice parameters of chrysoberyl and rutile, the two distances are d_{Ch} = 1.4453 nm and d_R = 1.4463 nm,
364 corresponding to six interatomic distances, $d'_{Al\text{-}Al}$ or $d'_{Ti\text{-}Ti}$, projected onto the interface from each
365 side. The misfit between the two crystal lattices for our $(120)_{Ch}|(103)_R$ interface can be calculated by
366 $\delta = 2\cdot|(d_{Ch} - d_R)/(d_{Ch} + d_R)|$ (Daneu *et al.* 2014). The resulting small misfit of δ = 0.069 % indicates that
367 chrysoberyl and rutile are almost perfectly matched at this particular interface. Unless the rutile is
368 orthorhombically deformed, a slightly worse coherence of the Ch|R interface with $\delta_\perp$ = 6.43 % is ex-
369 pected along the $[001]_{Ch}|[010]_R$ direction. This would be compensated by misfit dislocations along
370 the $(120)_{Ch}|(103)_R$ interface in perpendicular direction at half of the Vernier period of a misfit, ½·D =
371 3.55 nm, after which 15 oxygen-oxygen interplanar distances along $[010]_R$ direction in the larger ru-
372 tile lattice would be compensated by an additional oxygen plane along $[001]_{Ch}$ direction of the host-
373 ing chrysoberyl lattice to compensate for the misfit (Daneu *et al.* 2014).

374 Based on the reconstructed unit-cell of rutile and its relation to chrysoberyl the following orienta-
375 tion relationship between chrysoberyl and rutile precipitates can be written:

376 $$[001]_{Ch}\{120\}_{Ch} \parallel [010]_R\{103\}_R$$

377 producing two unique orientations of rutile precipitates within the chrysoberyl matrix; illustrated in
378 simulated EDP of chrysoberyl with the two possible orientations of rutile (Figure 8f). At the V- or L-
379 junctions, such as shown in Figure 8b, the rutile domains $R_1|R_2$ are enclosing the angles of 122.57° or
380 57.43° and produce semi-coherent (101)- and (301)-type twin boundaries through impingement.

381 This relationship was used for the construction of chrysoberyl-rutile-chrysoberyl super-cell in
382 HRTEM image simulations. For interface analysis, an experimental image of chrysoberyl with 2-nm-
383 thick precipitate of rutile was used (Figure 9a). In the model, the rutile interlayer was placed at the

centre of the orthorhombic super-cell with the following dimensions: $A = 8 \cdot d_{120Ch} + 21 \cdot d_{103R} + 8 \cdot d_{120Ch}$ = 7.6872 nm, $B = 21 \cdot d_{2\bar{3}0Ch} \approx 75 \cdot d_{80\bar{1}R}$ = 4.3359 nm and $C = d_{001Ch}$ = 0.4431 nm, containing 1896 atoms. The *A*-dimension was chosen large to include the rutile interlayer and sufficient chrysoberyl for comparison with the experimental image, *B*-dimension was set to a triple of interface periodicity d_R, and for *C*-dimension one unit-cell along the crystallographic *c*-axis of chrysoberyl was necessary. Under selected imaging conditions, similar to those in Figure 5, the contrast of the rutile interlayer is characterized by simple pseudo-hexagonal pattern of white dots coinciding with the positions of Ti^{4+} atoms, characteristic for the $[010]_R$ zone axis. The chrysoberyl-rutile interface is characterized by intense white dots on the rutile slab with a period of $½ \cdot d_R$. The contrast features of the experimental HRTEM image, including the more intense dots at the rutile-chrysoberyl interface, are well reproduced by simulation (Figure 9b) using the structural model, shown in Figure 10. A closer look at the atomic model reveals why twice the distance between the intense white dots, marked in Figure 9, is needed to achieve the interface periodicity $d_R \approx d_{Ch}$. At this distance, a full structural coherence is achieved along the $(120)_{Ch}|(103)_R$ interface. Both structures are fitted into a close-packed hexagonal O-sublattice with the cations occupying different interstitial sites. While the model is yet energetically unrelaxed, it still well demonstrates the nature of intergrown rutile precipitates.

401 **Implications**

402 At present it remains unclear what triggers the formation of twin boundaries in chrysoberyl. Fur-
403 ther analysis of (130) twins, including the samples from other localities, will be necessary to verify a
404 possibility of chemically-induced twinning in chrysoberyl. As recently demonstrated on (301) and
405 (101) twins of rutile (Daneu *et al.* 2007b; Daneu *et al.* 2014), it may be possible that also twinning of
406 chrysoberyl is triggered by the nucleation and epitaxial overgrowth on a precursor with a hexagonal
407 or pseudo-hexagonal O-sublattice, such as BeO or α-Al_2O_3. Future work will necessitate atomic reso-
408 lution studies where attention must be paid to the presence of light elements, such as boron, and the
409 possible presence of growth precursors (alumina, beryllia) at the twin boundary. A similar type of V-
410 shaped twins of chrysoberyl in embedded in metamorphosed quartz-muscovite matrix have been de-
411 scribed from Hartford pegmatite in Maine (Palache 1924), Saratoga in New York, Miesling valley in
412 Austria and Rosendal in Finland, and we may expect a similar mechanism of twin formation.

413 Exsolution of rutile and formation of star-sapphires has been thoroughly studied in α-Al_2O_3 (*e.g.*
414 Phillips *et al.* 1980; Jayaram 1988), which offers possible explanations for the formation of rutile pre-
415 cipitates in chrysoberyl. The precipitation of TiO_2 most probably occurred on cooling of Ti^{4+}-rich
416 chrysoberyl solid solutions when supersaturation conditions are reached and a phase separation pro-
417 cess takes place. Nanostructural analysis of rutile exsolutions has shown that the *c*-axis of rutile is
418 oriented in such a way that the channels along this direction are providing shortest pathways for cat-
419 ion diffusion that allow lateral growth of the precipitates after their nucleation as long as Ti^{4+} ions
420 continue to segregate from the hosting chrysoberyl matrix to form rutile. On further cooling, elastic
421 accommodation of the rutile structure, as determined by quantitative HRTEM analysis, was probably
422 driven by a temperature dependent contraction of chrysoberyl lattice parameters, offering interest-
423 ing implications for determination of rutile exsolution temperature, which would help to better un-
424 derstand the dynamics of geochemical processes during the crystallization of chrysoberyl.

425

426 **Acknowledgements**

427 The present work is a part of the Ph.D. thesis of S. Drev financed by the Slovenian Research Agen-
428 cy under the contract No. 1000-11-310205. This research was conducted within the frame of the na-
429 tional research project No. J1-4167: »Twinning, epitaxy and phase transformations in minerals«. The
430 authors acknowledge Luiz Menezes (Belo Horizonte, BR) for providing the chrysoberyl specimens and
431 the locality information.

References

Anderson, B.W., C.J. Payne and G.F. Claringbull (1951) Taaffeite, a new beryllium mineral, found as a cut gemstone. Mineralogical Magazine 29, 765-772.

Blöchl, P.E. (1994) Projector augmented-wave method. Physical Review B, 50, 17953.

Bragg, W.L. and G.B. Brown (1926) Die Kristallstruktur von Chrysoberyll. Zeitschrift für Kristallographie 63, 122-143.

Cemič, L., K. Langer and G. Franz (1986) Experimental determination of melting relationships of beryl in the system $BeO–Al_2O_3–SiO_2–H_2O$ between 10 and 25 kbar. Mineralogical Magazine 50, 55-61.

Cornejo, C. and A. Bartorelli (2010) Minerals and precious stones of Brazil. Solaris cultural publications, São Paulo (Brazil).

Černý, P. (2002) Mineralogy of beryllium in granitic pegmatites. Reviews in Mineralogy and Geochemistry 50, 405-444.

Daneu, N., A. Rečnik, T. Yamazaki and T. Dolenec (2007a) Structure and chemistry of (111) twin boundaries in $MgAl_2O_4$ spinel crystals from Mogok (Burma). Physics and Chemistry of Minerals 34, 233-247.

Daneu, N., H. Schmid, A. Rečnik and W. Mader (2007b) Atomic structure and formation mechanism of (301) rutile twins from Diamantina (Brazil). American Mineralogist 92, 1789-1799.

Daneu, N., A. Rečnik and W. Mader (2014) Atomic structure and formation mechanism of (101) rutile twins from Diamantina (Brazil). American Mineralogist 99, 612-624.

Davies, P.K. and M. Akaogi (1983) Phase intergrowths in spinelloids. Nature 305, 788-790.

Dalton de Souza J., Kosin M., Melo R.C., Santos R. A., Teixeira L. R., Sampaio A. R., Guimarães J. T., Vieira Bento R., Borges V. P., Martins A. A. M., Arcanjo J. B., Loureiro H. S. C., Angelim L. A. A. 2003. Mapa geológico do Estado da Bahia – Escala 1:1.000.000. Salvador: CPRM, 2003. Versão 1.1. Programas Carta Geológica do Brasil ao Milionésimo e Levantamentos Geológicos Básicos do Brasil (PLGB). Convênio de Cooperação e Apoio Técnico - Científico CBPM/CPRM.

Drev, S., A. Rečnik and N. Daneu (2013) Twinning and epitaxial growth of taaffeite-type modulated structures in BeO-doped $MgAl_2O_4$, CrystEngComm 15, 2640-2647.

Farrell, E.F., J.H. Fang and R.E. Newham (1963) Refinement of the chrysoberyl structure. American Mineralogist 48, 804-810.

Farrell, E.F. and J.H. Fang (1964) Flux growth of chrysoberyl and alexandrite. Journal of the American Ceramic Society 47, 274-276.

Franz, G. and G. Morteani (1984) The formation of chrysoberyl in metamorphosed pegmatites. Journal of Petrology 25, 27-52.

Giannozzi, P., S. Baroni, N. Bonini, M. Calandra, et al. (2009) QUANTUM ESPRESSO: A modular and open-source software project for quantum simulations of materials. Journal of Physics: Condensed Matter 21, 395502.

Hazen, R.M. (1987) High-pressure crystal chemistry of chrysoberyl, $BeAl_2O_4$: Insights on the origin of olivine elastic anisotropy. Physics and Chemistry of Minerals 14, 13-20.

Hazen, R.M. and L.W. Finger (1987) High-temperature crystal chemistry of phenakite (Be_2SiO_4) and chrysoberyl ($BeAl_2O_4$). Physics and Chemistry of Minerals 14, 426-434.

Henderson, C.M.B., K.S. Knight and A.R. Lennie (2009) Temperature dependence of rutile (TiO_2) and geikielite ($MgTiO_3$) structures determined using neutron powder diffraction. The Open Mineralogy Journal, 3, 1-11.

Jayaram, V. (1988) The precipitation of alpha-TiO_2 from supersaturated solutions of Ti in alumina (Crystal structure and morphology). Philosophical Magazine A, 57, 525-542.

Kleebe, H.J. and S. Lauterbach (2008) Exaggerated grain growth in bixbyite via fast diffusion along planar defects. Crystal Research and Technology 43, 1143-1149.

Khranenko, G.G. and A.M. Yurkin (2000) Controlled nucleation of chrysoberyl crystals in a flux system. Inorganic Materials 36, 171-172.

Lottermoser, W., G.J. Redhammer, S.U. Weber, F.J. Littterst, G. Tippelt, S. Dlugosz, H. Bank, G. Amthauer and M. Grodzicki (2011) The electric field gradient in natural iron-doped chrysoberyl Al_2BeO_4 and sinhalite $MgAlBO_4$ single crystals. Physics and Chemistry of Minerals 38, 787-799.

Mitchell, T.E. and J.M. Marder (1982) Precipitation in cat's-eye chrysoberyl. Proceedings of the Electron Microscopy Society of America (EMSA).

Moor, R., W.F. Oberholzer and E. Gübelin (1981) Schweizerische Mineralogische und Petrographische Mitteilungen 61, 13-21.

Palache, C. (1924) The chrysoberyl pegmatite of Hartford, Maine. American Mineralogist 9, 217-221.

Palache, C., H. Berman and C. Frondel (1944) The system of mineralogy. Vol. I – elements, sulfides, sulfosalts and oxides. 7th Edition. John Wiley&Sons Inc., London (UK).

Perdew, J.P. and A. Zunger (1981) Self-interaction correction to density-functional approximations for many-electron systems. Physical Review B, 23, 5048.

Phillips, D.S., Heuer, A.H. and Mitchell, T.E. (1980) Precipitation in star sapphire – II. Elastic accommodation of the precipitate. Philosophical Magazine A, 42, 405-416.

Rečnik, A. and N. Daneu (2012) The atomic-scale aspects of twinning and polytypism in minerals. Acta Mineralogica-Petrographica – Abstract Series (Szeged) 7, 32-37.

Rose G. (1839) Ueber den Chrysoberyll vom Ural. Annalen der Physik und Chemie 48, 570-573.

Scalvi, R.M.F., M.S. Li, and L.V.A. Scalvi (2003) Annealing effects on optical properties of natural alexandrite. Journal of Physics: Condensed Matter 15, 7437-7443.

Schmetzer, K. (1981) Zur Mineralogie ternärer Oxide im System BeO-MgO-Al_2O_3. Naturwissenschaften 68, 471-472.

Schmetzer, K. (1983) Crystal chemistry of natural Be-Mg-Al oxides: taaffeite, taprobanite and musgravite. Neues Jahrbuch für Mineralogie - Abhandlungen 146, 15-28.

Schmetzer, K. (2010) Russian Alexandrites. Schweizerbart Science Publishers, Stuttgart (Germany).

Schrauf, A. (1877) Atlas der Kristall-Formen des Mineralreiches. Wilhelm Braumüller Verlag. Wien. Band I, Taf. XLV, Fig. 10.

Swanson, H.E., M.I. Cook, T. Isacs, E.H. Evans (1960) Standard X-ray diffraction powder patterns: Chrysoberyl ($BeAl_2O_4$). National Bureau of Standards. Washington. Circular 539, Vol. 9, 10-12.

Šrot, V., A. Rečnik, C. Scheu, S. Šturm and B. Mirtič (2003) Stacking faults and twin boundaries in sphalerite crystals from the Trepča mines in Kosovo. American Mineralogist 88, 1809-1816.

Tabata, H., E. Ishii and H. Okuda (1974) Growth and morphology of chrysoberyl single crystals. Journal of Crystal Growth 24/25, 656-660.

Takeuchi, Y. (1997) Tropochemical cell-twinning. A structure building mechanism in crystalline solids. Terra scientific publishing company, Tokyo.

Weber, S.U., M. Grodzincki, W. Lottermoser, G.J. Redhammer, G. Tippelt, J. Ponahlo and G. Amthauer (2007) ^{57}Fe Mössbauer spectroscopy, X-ray single-crystal diffractometry, and electronic structure calculations on natural alexandrite. Physics and Chemistry of Minerals 34, 507-515.

519 **List of Figure Captions**

520 **Figure 1**. Morphology of V-shaped twin of chrysoberyl from Pratinhas, Brazil. (**a**) The twin boundary follows a
521 (130) contact plane, splitting the crystal on two mirror-symmetric halves, with the two domains enclosing an
522 angle of ~59.5°. (**b**) Schematic illustration of (130) twin of chrysoberyl with the following forms: **a**(100), **b**(010),
523 **c**(001), **i**(110), **o**(111), **r**(031) and **π**(131). Indexing is according to the space group Pmnb (*see* the crystallog-
524 raphy section). Rectangular area indicates the approximate position of cutting of the TEM specimen.

525 **Figure 2**. Comparison between spinel, taaffeite and chrysoberyl structures in unified orientation, where (111)-
526 axis of spinel is parallel to the pseudo-hexagonal axis of taaffeite and chrysoberyl. Be-rich (111) twin boundary
527 in spinel can be described as *hcp* stacking disruption of the *ccp* spinel lattice accompanied by incorporation of
528 Be. Periodic modulations of the two sequences generate polysomatic minerals of taaffeite series, where
529 chrysoberyl is Be-rich end-member. Unlike in chrysoberyl, the crystallographic *c*-axis of taaffeite is aligned par-
530 allel with the pseudo-hexagonal axis of the structure. Yellow lines indicate the stacking of the O-sublattice.

531 **Figure 3**. X-ray powder diffraction analysis of chrysoberyl crystal from Pratinhas. (**a**) Experimental pattern with
532 red arrows indicating positions of rutile reflections. (**b**) Indexed simulated XRD pattern of chrysoberyl after
533 Rietveld analysis of experimental data. (**c**) Indexed simulated XRD pattern of rutile inclusions. New cell parame-
534 ters for chrysoberyl, refined in *Pmnb* (62) space group, are listed in the upper right corner.

535 **Figure 4**. TEM and electron diffraction study of (130) twin boundary in chrysoberyl from Pratinhas. (**a**) Bright-
536 field TEM image of the twin boundary intersecting thin crystal part populated with oriented TiO_2 precipitates.
537 Electron diffraction pattern (EDP) recorded in domain I is rotated by ~59.5° with respect to that of domain II,
538 which exactly corresponds to the angle enclosed by the a-axes (marked by arrows), distinctive for (130) twin.
539 (**b**) Twin boundary step to adjacent (130) planes. Note the moiré pattern in the transition area, produced by
540 overlapping crystals in twin orientation. (**c**) Simulated EDP for (130) twin of chrysoberyl in [001] orientation
541 based on crystallographic data obtained from Rietveld refinement.

542 **Figure 5**. HRTEM study of (130) twin boundary in chrysoberyl from Pratinhas. (**a**) Experimental HRTEM image
543 recorded in ~18 nm thick crystal at defocus value of f = -59 nm. The twin boundary is not straight, but slightly
544 climbs from left to right by making ½·d_{130} steps to the adjacent (260) planes. In straight sections, the boundary
545 shows periodic features after every four ($\bar{1}$10) planes along the interface (*see* outlined super-cells). Series of
546 periodic cells were used to produce an average experimental image with enhanced contrast, shown as the last
547 inset of the series (avr). (**b**) Close-up of processed experimental image, with the height of 2-times the periodic
548 sequence along the interface. In the lower part of the image wavy chains produced by undulating O-columns is
549 outlined with black ripples. Black areas inbetween correspond to the positions of Be-columns. I and II denote

two characteristic atomic clusters along the interface. (**c**) Simulated HRTEM image based on the atomic model produced by mirror operation over an (130) lattice plane with overlaid atomic positions (O – red, Al – grey, Be – green), calculated for experimental electron-optical conditions: spherical aberration C_s = 0.8 mm, spread of focus Δf = 8 nm, and beam convergence θ_c = 1.2 mrad. (**d**) Simulated HRTEM image based on DFT refined atomic model with shifted Be and O atoms in Cluster-I, and displaced Be atoms to the neighboring tetrahedral sites in Cluster-II (*see* the comparison between the unrelaxed and relaxed structural models in Figure 6).

Figure 6. DFT relaxed atomic structure of (130) twin boundary in chrysoberyl, viewed along $[001]_{ch}$ projection. Like in chrysoberyl, the periodicity along the super-cell *C*-axis is attained after two O-layers (shown separately for clarity), along the *B*-axis super-cell is periodic after four $(\bar{1}10)$ planes, whereas along the *A*-axis, running normal to the $(130)_{ch}$ twin boundary plane (red vertical line), the super-cell has no periodicity. Major atomic displacements are indicated by black arrows. Yellow dotted rectangles outline Cluster-I and Cluster-II.

Figure 7. EDS analysis of bulk chrysoberyl crystal, twin boundary and Ti-rich precipitate. Hosting chrysoberyl contains 0.56 ± 0.09 at% of Fe, whereas the twin boundaries are additionally enriched in Ti.

Figure 8. TEM study of anisotropic rutile precipitates in chrysoberyl from Pratinhas. (**a**) Two rutile orientations are observed (R_1 and R_2). (**b**) L-shaped cluster composed of two impinging rutile precipitates enclosing an angle of 98.7°. (**c**) Isolated rutile precipitate. In addition, small xenomorphic grains of faulted rutile are present (*see* the inset). The magnification in all three situations is identical for comparison. (**d**) Structural analysis of chrysoberyl-rutile (Ch|R_1) interface. Crystallographic axes of chrysoberyl and rutile are used to determine the orientation relationship $[001]_{Ch}(120)_{Ch} \parallel [010]_R(103)_R$. Real space 4x4 unit-cells are outlined in yellow. (**e**) Fast Fourier transform (FFT) of the HRTEM image from Fig. 8b displaying additional reflections from rutile R_1 and R_2 precipitates (indicated by arrows). (**f**) Reconstructed EDP of chrysoberyl and rutile precipitates calculated with lattice parameters of deformed rutile from the HRTEM analysis (Fig. 8d), with $(120)_{Ch} \parallel (103)_{R1}$ and $(1\bar{2}0)_{Ch} \parallel (103)_{R2}$. Reciprocal 2x2 unit-cells are outlined (chrysoberyl – grey, R_1 – red, R_2 – blue).

Figure 9. HRTEM analysis of rutile precipitates in chrysoberyl. (**a**) HRTEM image recorded under similar imaging conditions as the image in Fig. 5. The experimental image was average-filtered along the interface using the period of d_R (or d_{Ch}) to enhance the boundary features. (**b**) Simulated HRTEM image based on the chrysoberyl-rutile-chrysoberyl atomic model shown in Fig. 10. The super-cell is outlined at the centre.

Figure 10. Rigid atomic model of a rutile slab in chrysoberyl. The two structures are coherently intergrown owing to their common hexagonal close-packed O-sublattice. Be^{2+} ions occupy tetrahedral, while Al^{3+} and Ti^{4+} ions occupy the octahedral interstices. Periodic unit along the $(120)_{Ch}|(103)_R$ interface is marked by arrows.

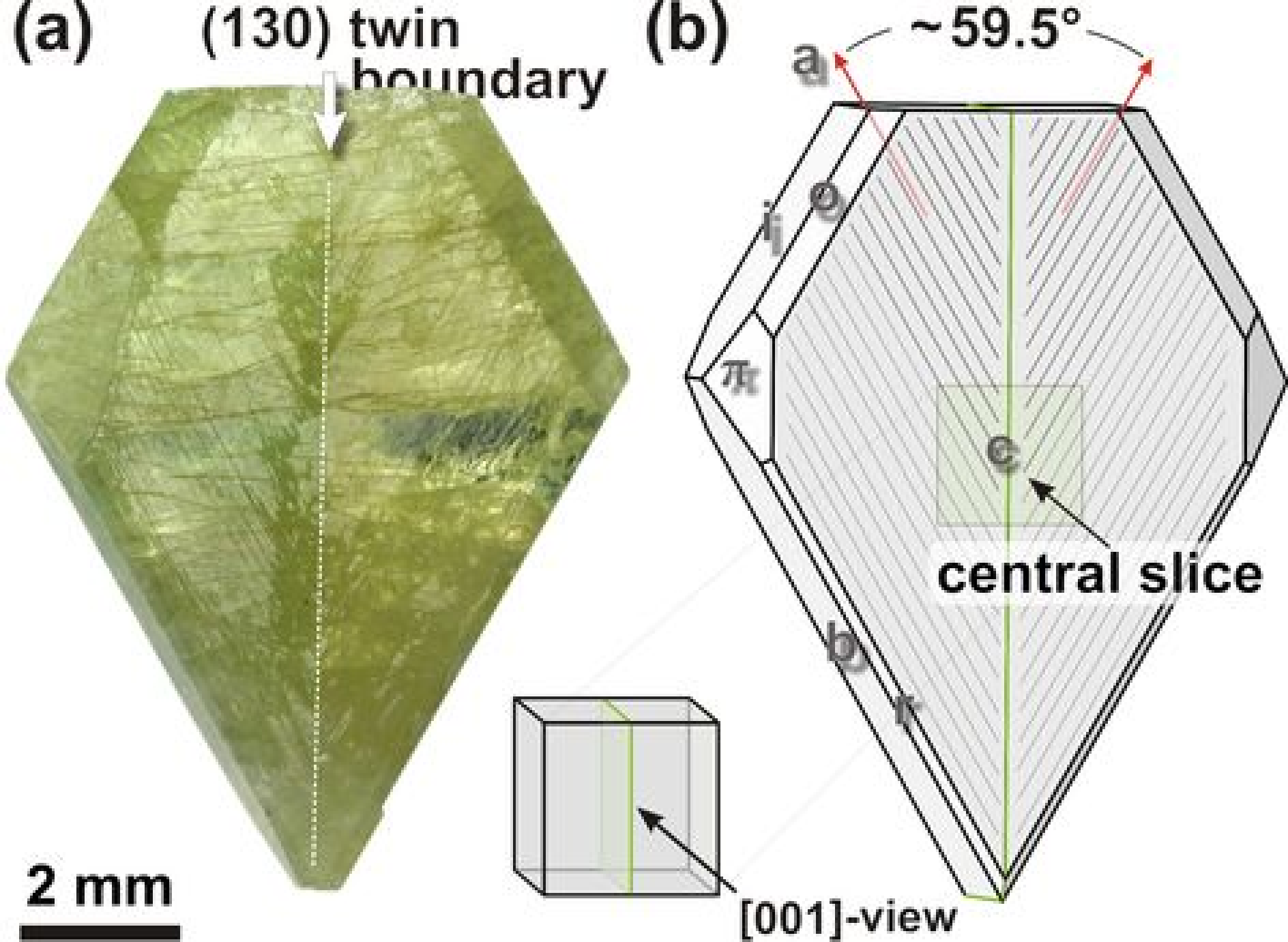
(a)
(130) twin boundary
2 mm
(b)
~59.5°
a
i
e
π
c
central slice
b
f
[001]-view

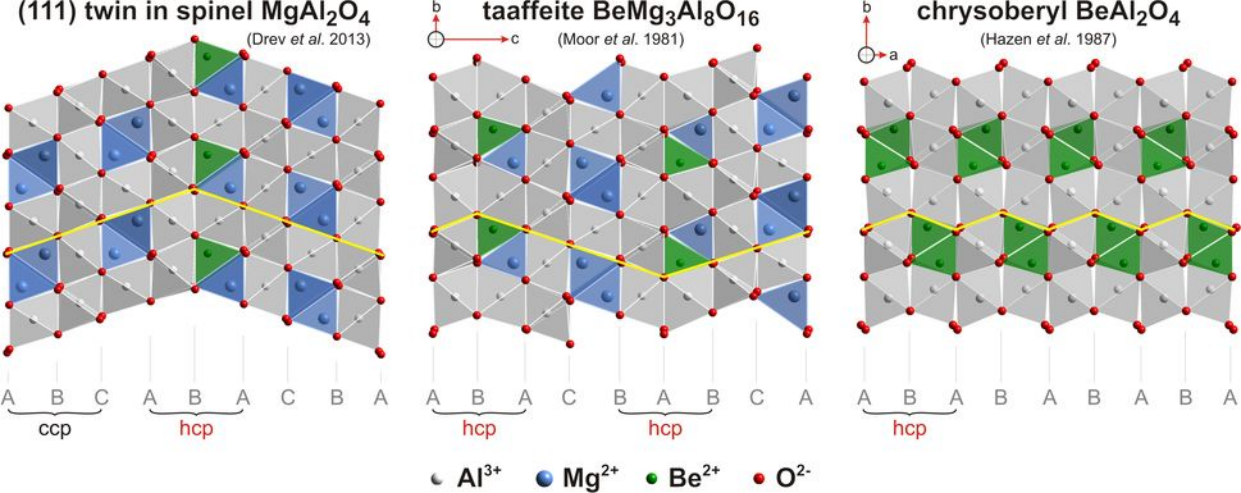
(111) twin in spinel $MgAl_2O_4$
(Drev et al. 2013)
taaffeite $BeMg_3Al_8O_{16}$
(Moor et al. 1981)
chrysoberyl $BeAl_2O_4$
(Hazen et al. 1987)
b
c
a
A B C A B A C B A
ccp
hcp
A B A C B A B C A
hcp
hcp
A B A B A B A B A
hcp
Al^{3+} Mg^{2+} Be^{2+} O^{2-}

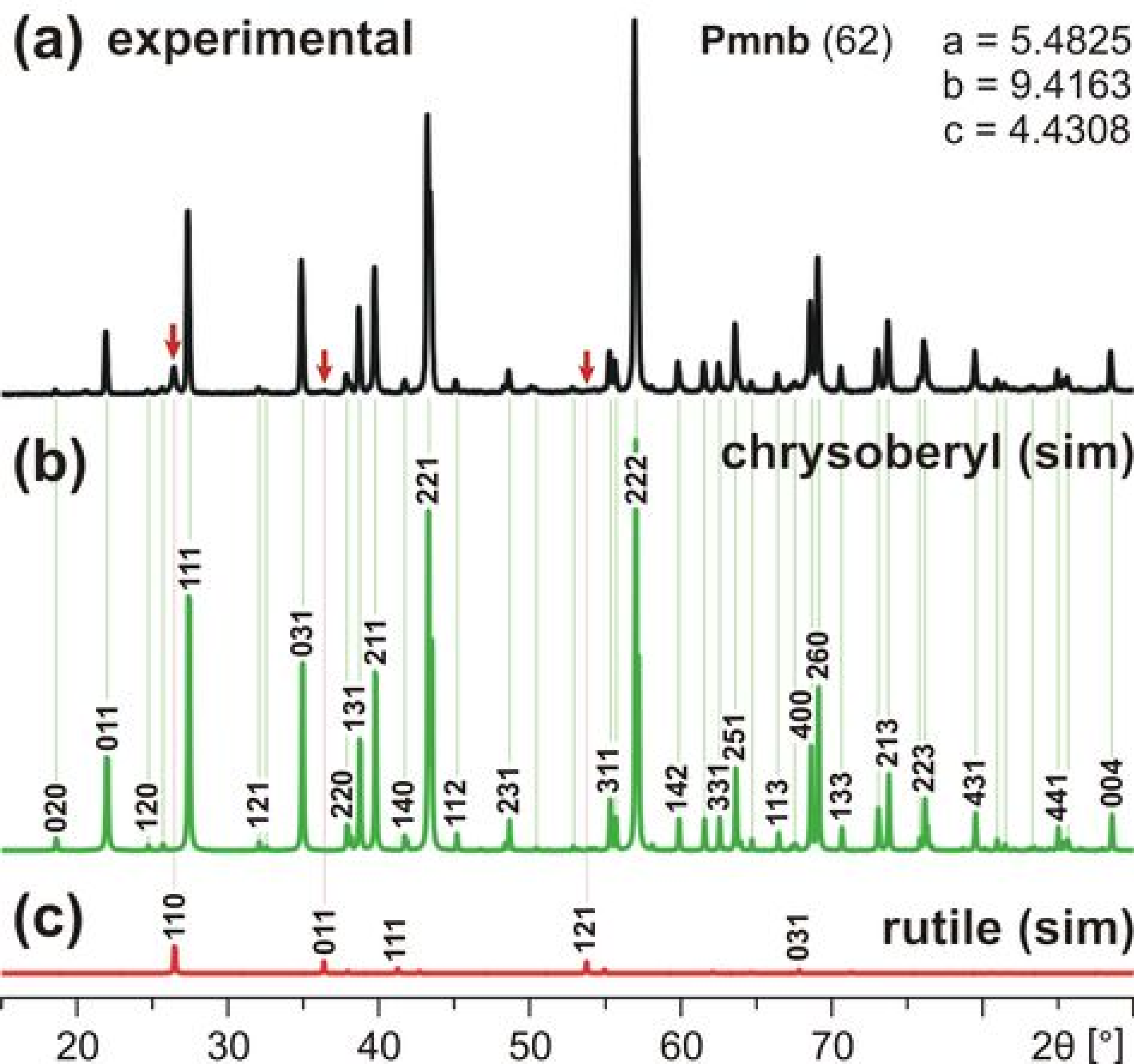
(a) experimental
Pmnb (62)
a = 5.4825
b = 9.4163
c = 4.4308
(b)
chrysoberyl (sim)
020
011
120
111
121
031
220
131
211
140
221
112
231
311
222
142
331
251
113
400
260
133
213
223
431
441
004
(c)
rutile (sim)
110
011
111
121
031
20
30
40
50
60
70
2θ [°]

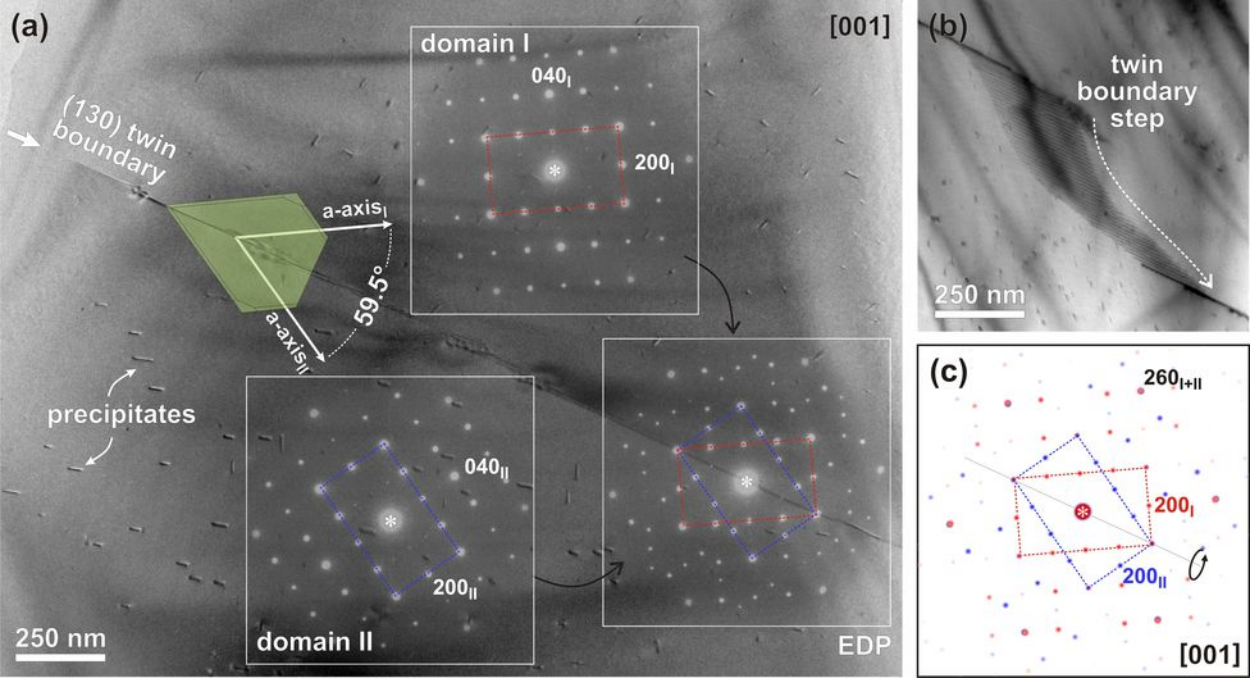
(a)
[001]
domain I
040I
200I
(130) twin boundary
a-axisI
59.5°
a-axisII
precipitates
040II
200II
250 nm
domain II
EDP
(b)
twin boundary step
250 nm
(c)
260I+II
200I
200II
[001]

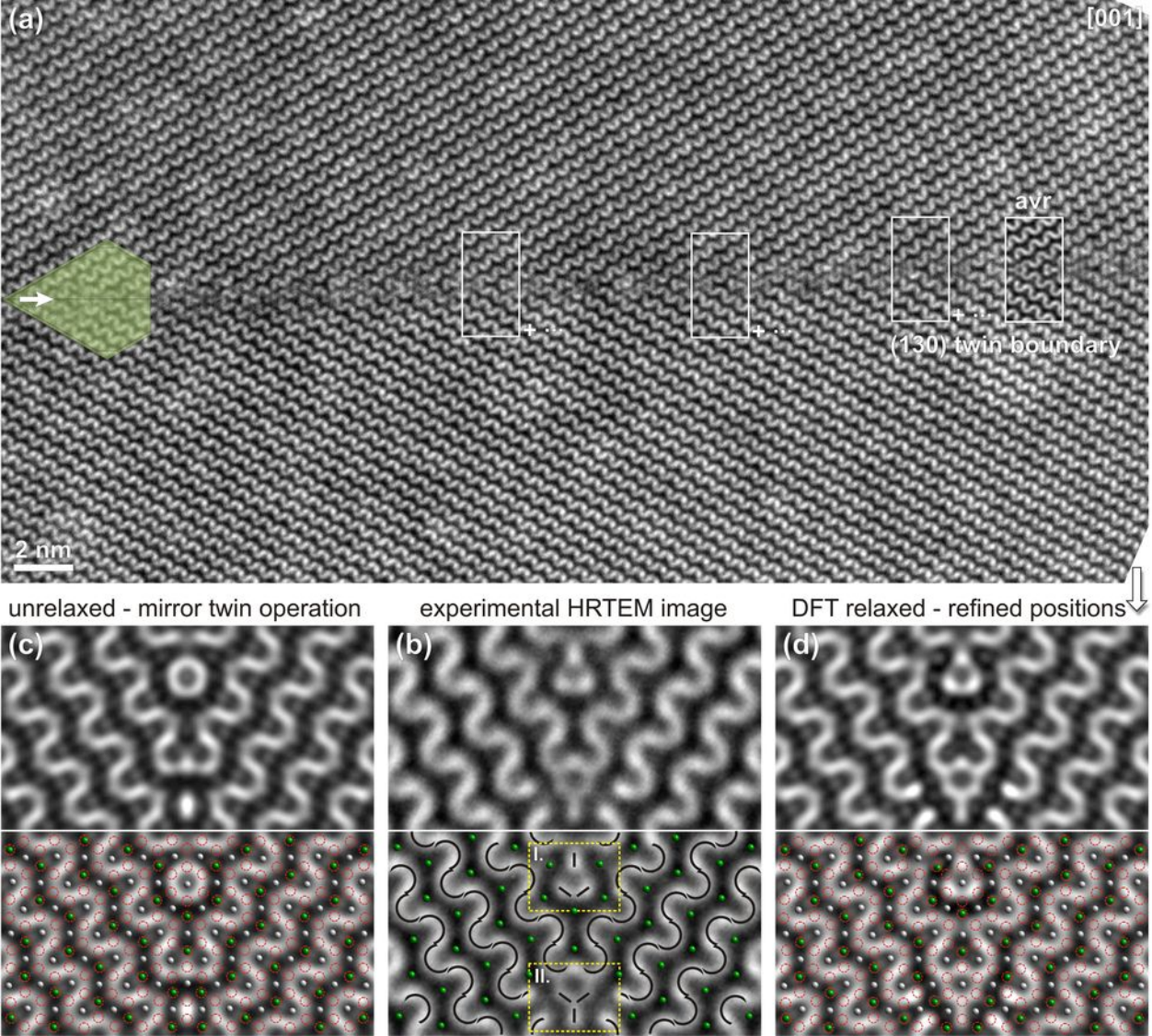
(a)
[001]
avr
(130) twin boundary
2 nm
unrelaxed - mirror twin operation
experimental HRTEM image
DFT relaxed - refined positions
(c)
(b)
(d)
I.
II.

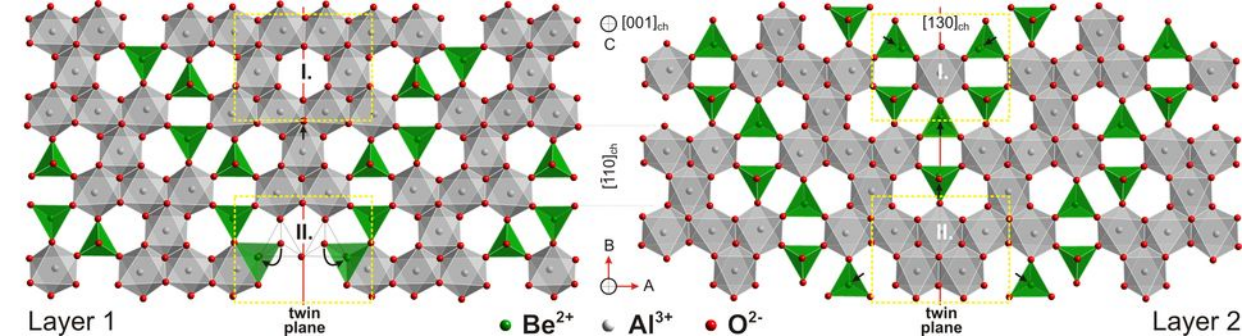
I.
II.
Layer 1
twin plane
Be2+
Al3+
O2-
[001]ch
C
[130]ch
I.
[110]ch
B
A
II.
twin plane
Layer 2

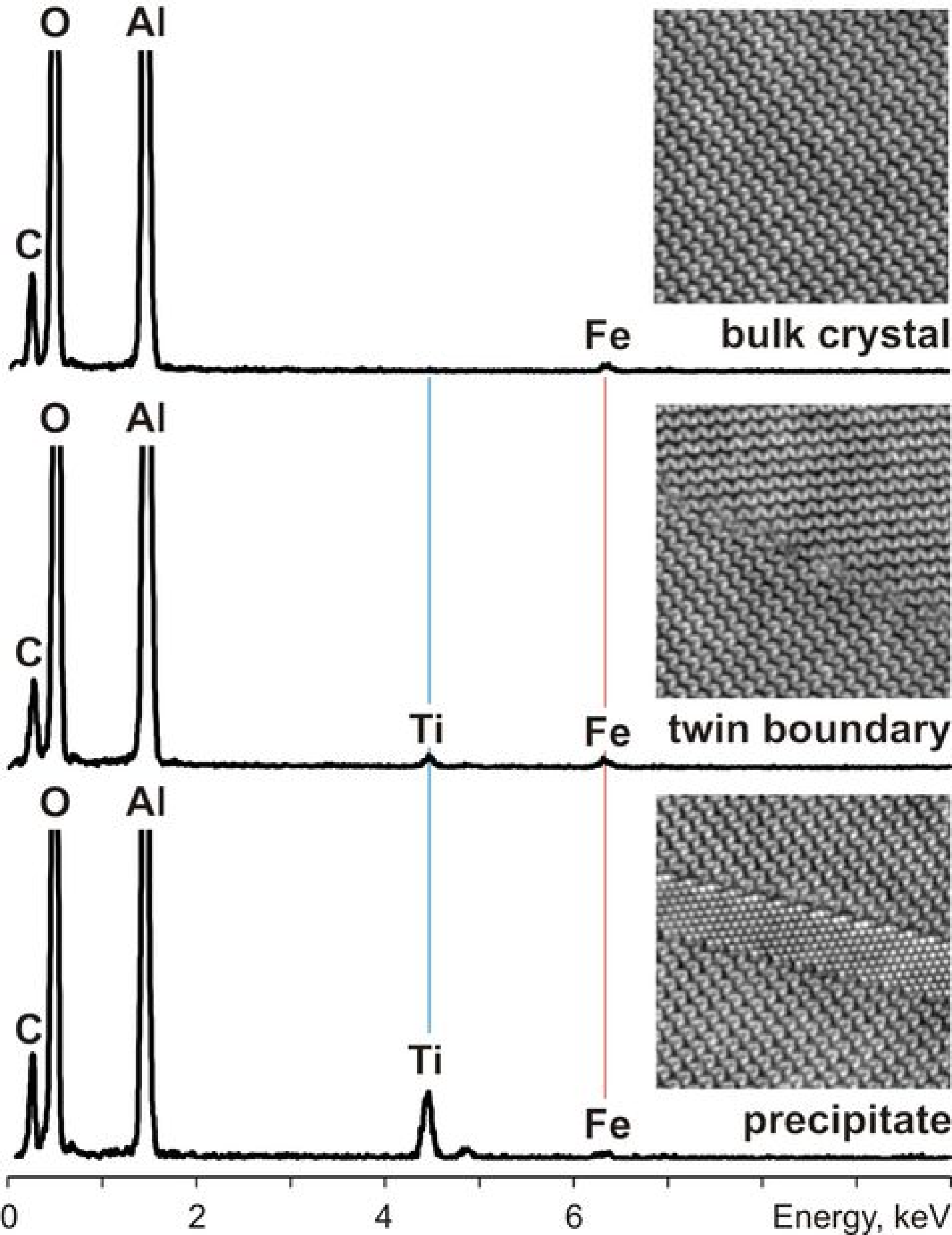
O
Al
C
Fe
bulk crystal
O
Al
C
Ti
Fe
twin boundary
O
Al
C
Ti
Fe
precipitate
0
2
4
6
Energy, keV

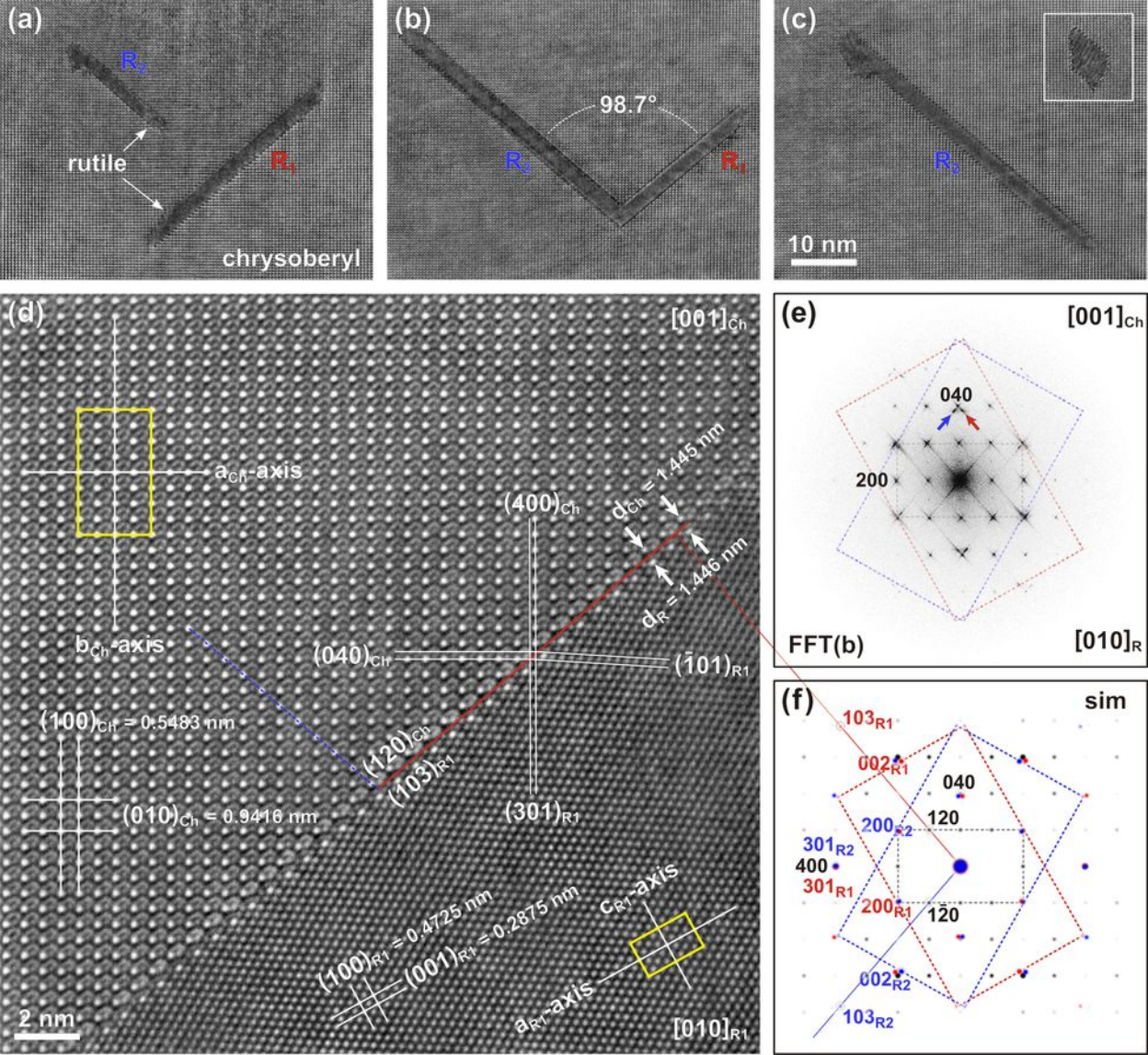
(a)
R2
rutile
R1
chrysoberyl
(b)
98.7°
R2
R1
(c)
R2
10 nm
(d)
[001]Ch
aCh-axis
bCh-axis
(400)Ch
dCh = 1.445 nm
dR = 1.446 nm
(040)Ch
(101)R1
(100)Ch = 0.5483 nm
(120)Ch
(103)R1
(010)Ch = 0.9416 nm
(301)R1
(100)R1 = 0.4725 nm
(001)R1 = 0.2875 nm
cR1-axis
aR1-axis
[010]R1
2 nm
(e)
[001]Ch
040
200
FFT(b)
[010]R
(f)
sim
103R1
002R1
040
120
200R2
301R2
400
301R1
200R1
120
002R2
103R2

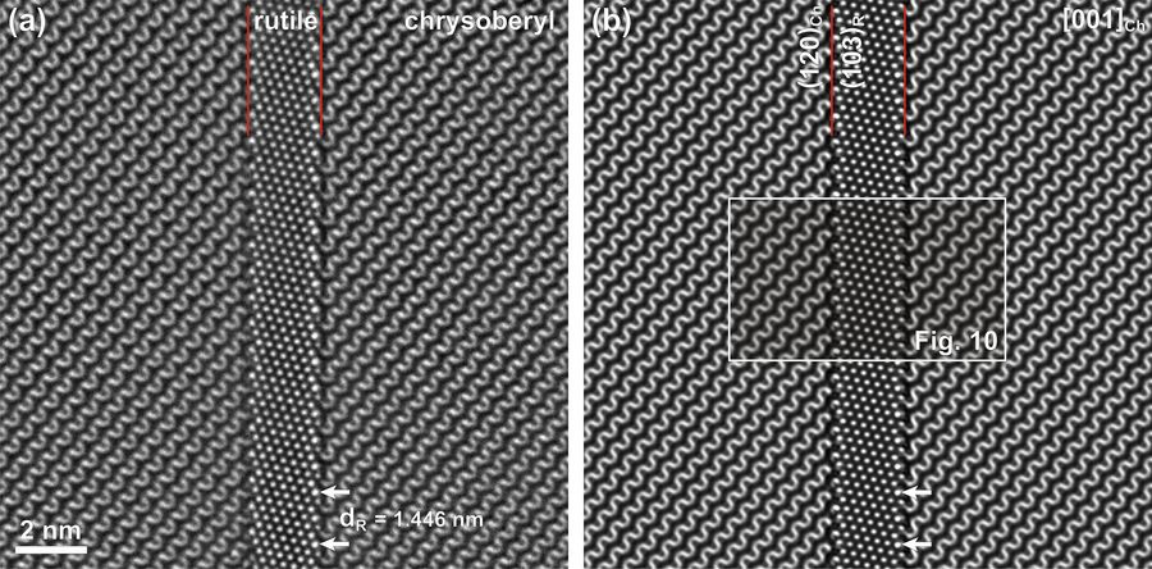
(a)
rutile
chrysoberyl
2 nm
d_R = 1.446 nm
(b)
$[001]_{Cb}$
$(120)_{Cb}$
$(103)_R$
Fig. 10

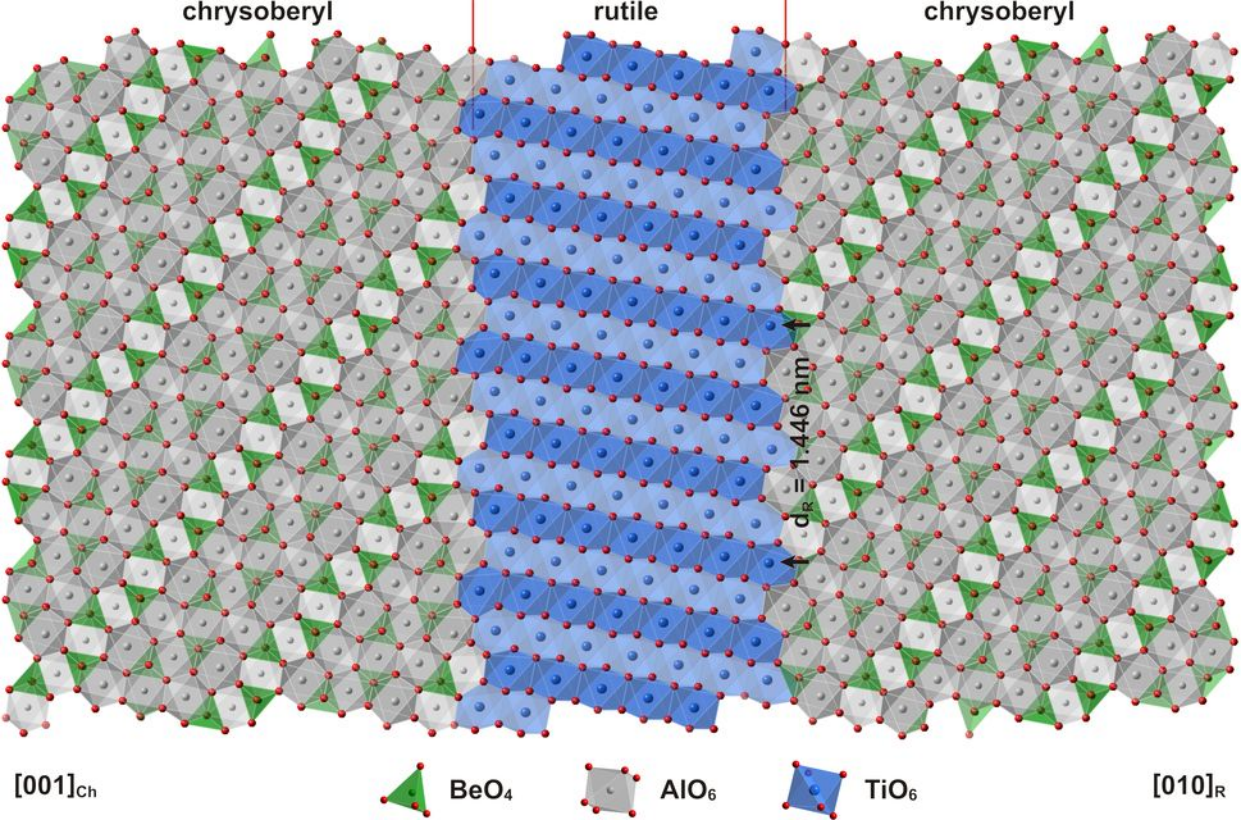
chrysoberyl
rutile
chrysoberyl
d_R = 1.446 nm
$[001]_{Ch}$
BeO_4
AlO_6
TiO_6
$[010]_R$